A Statistical Descriptor Based Volume-Integral Micromechanics model of Heterogeneous Material with Arbitrary Inclusion Shape

Zeliang Liu[1], John A. Moore[2], Saad M. Aldousari[3], Hassan S. Hedia[3], Saeed A. Asiri[3], Wing Kam Liu[2,4,*]

[1]*Theoretical and Applied Mechanics, Northwestern University, Evanston, IL, 60208, USA*

[2]*Department of Mechanical Engineering, Northwestern University, Evanston, IL, 60208, USA*

[3]*Department of Mechanical Engineering, King Abdulaziz University, Jeddah, KSA*

[4]*Distinguished Scientists Program Committee at King Abdulaziz University (KAU), Jeddah, Saudi Arabia*

Abstract

A continuing challenge in computational materials design is developing a model to link the microstructure of a material to its material properties in both an accurate and computationally efficient manner. In this paper, such a model is developed which uses image-based data from characterization studies combined with a newly developed **s**elf-consistent **v**olume-**i**ntegral **m**icromechanics model (SVIM) based on radial distribution function. It is observed that SVIM is able to capture the effective stress/strain distribution inside the inclusion, as well as the effects of volume fraction and nearest inclusion distance on the effective properties of heterogeneous material. More importantly, SVIM can be applied to inclusions with arbitrary shape through discretizing the inclusion domain, which is missing in traditional mean-field micromechanics models. For both 2-Dimensional (2D) and 3-Dimensional (3D) problems with identical circular and spherical inhomogeneities, SVIM's capability of predicting effective elastic properties is validated against experiments and direct numerical simulations using finite element method (FEM). Finally, the effect of inclusion shape is predicted by SVIM.

Keywords: micro-mechanics, modulus and composites, finite element, materials design, statistical descriptors

1. Introduction

Computational modeling and design of materials is becoming increasingly widespread in the development of new advanced material system [1, 2]. As the properties of materials and the interaction between each microstructural phase become increasingly complex, traditional design processes relying on the experimental *Edisonian* trial-and-error approach can become intractable for finding the optimal designs. For a heterogeneous material, three major factors driving materials properties are phase compositions, geometry and their interaction. To better understand and improve materials behavior, a model is needed to take these statistical microstructural parameters and convert them to the desired properties of the macroscopic material.

Accuracy of the prediction and computational cost of the model are the two critical aspects that should be considered for the materials design or optimization process. The desired model is one that accurately predicts the properties of the material with low computational effort, and is the goal of this paper. We starts from the statistical description of the microstructure based on imaging techniques such as scanning electron microscope (SEM), transmission electron microscopy (TEM), Local-Electrode Atom-probe (LEAP) tomography and/or X-ray diffraction. Two representative volume element (RVE) modeling

* Corresponding author: Tel: +1 847 491 7094
Email address: w-liu@northwestern.edu (W.K. Liu).

methods are then investigated in this paper: direct numerical simulation (DNS) and self-consistent volume-integral micromechanics (SVIM) based on statistical descriptors. These methods can be utilized to determine the effective properties of heterogeneous materials. In the DNS method, replications of RVEs are reconstructed with the same statistical descriptors as the original experimental image and simulated using finite element method (FEM). However, the DNS can be extremely slow when modeling a complex heterogeneous material on the scale of RVE, whose size in 3D should exceed at least 15 times of the particle diameter for high accuracy which has been proved both analytically [3] and experimentally [4]; this RVE size makes DNS prohibitive from a design perspective. A more efficient way to predict the RVE properties is to put the statistical information directly into the SVIM model proposed in this paper.

In the present work, a new self-consistent volume-integral micromechanics model (SVIM) is developed for two-phase heterogeneous material with identical arbitrarily shaped inclusion both in 2D and 3D, and is validated against DNS and experiments. We first discuss the image-based material characterization and reconstruction, as well as the RVE modeling using FEM. Then we explain in detail how to incorporate the statistical descriptors into the volume integral equation, and how to derive the self-consistent equation. Finally, the self-consistent equation is solved iteratively and the results are compared with DNS of the RVE using FEM and experiments.

2. Background

Material characterization (i.e. SEM., TEM, LEAP, etc.) enables the mathematical descriptions of composite and heterogeneous alloys with complex morphology by creating a strong line between these mathematical models and the true microstructure of the material. An example of such a model is that of a nanoparticle filled polymer system studied by Deng et al [5] and Xu et al. [6, 7], where 3D microstructures were reconstructed based on the statistical descriptors (to reduce the need for time-consuming imaging techniques) and finite element analysis (FEA) was performed to determine the properties of these virtual materials. This FEA however, becomes increasingly expensive as the size and/or complexity of the RVE (and thus the number of needed elements) increases.

Alternative DNS method to FEM can be Fast Fourier Transform (FFT)-based method for periodic structure, which is reported faster than FEM for elastic problem [8]. Since FFT is used, uniform mesh is required. For a 3D problem, assume the discretizing number at each dimension is N, then the complexity of FFT on the $N \times N \times N$ mesh is $O(N^3 \, log \, N^3)$ in theory. If we keep the resolution of the discretization, the computational time will increase at least cubic with the RVE size.

In order to decrease the computational cost of DNS, Moore, et al. [9] divided a similar RVE into several smaller Statistical Volume Elements (SVEs) whose properties were predicted by a modified Mori-Tanaka [10] and Halpin-Tsai [11] (based on self-consistent model) micromechanics model, and each SVE's properties serves as element material parameters in an FEA of the total RVE [9]. A significant improvement of computation speed is reported, but the convergence of the properties is not guaranteed for small SVEs because incorrect boundary conditions were used (they assume RVE type boundary conditions for the SVE's) along with insufficient statistical information. Despite these shortcomings, Moore's work showed a promising and fast multiscale modeling framework based on combining FEM with analytical micromechanics methods. To deal with complex geometries characterized by several statistical descriptors, a more advanced micromechanics model than those found in traditional micromechanics methods is needed. Such a method will be useful as a constitutive equation in multiscale FEM simulations, as well as faster RVE simulation method for materials design optimization.

From variation principles, several bounds on elastic properties can be derived for isotropic two-phase materials. The most popular ones are the Hashin and Shrikman's lower and upper bounds (HS-LB and

HS-UB respectively) which only depend on the secondary phase volume fraction [12, 13]. However, these bounds can only provide an interval for the exact solution. When the contrast between the properties of the matrix and inhomogeneities becomes high, the gap between the upper and lower bounds is too large to provide a useful prediction.

Rather than giving the bounds, other micromechanics methods aim to approximate the values of elastic properties. The work done by Eshelby gives the exact solution of the stress field for one ellipsoidal inclusion in an infinite matrix [14]. For multi-inclusion problems, several methods have been proposed following Eshelby's work. Two typical methods are Mori-Tanaka [10] and the self-consistent method [15] based on the mean-field approximation. Rather than explicitly considering the interactions between the inclusions, an "effective" matrix was introduced to account for the average effects from the matrix and surrounding inclusions [10, 15, 16]. In this case, the effects from the distributions of the inclusions, such as the nearest inclusion distance effect discussed in Section 6.2, cannot be captured by these methods. In the work proposed by Ju and Chen [17, 18], probabilistic pairwise inclusion interactions were coupled into an ensemble-volume average equation and it was demonstrated that the Mori-Tanaka method coincides with the Hashin and Shrikman's lower bound. However, their multi-inclusion model is based on the solution to the problem with only two inclusions in the matrix, and the superposition of stress field is not guaranteed for multi-inclusion problems. Moreover, all the above micromechanics methods only work for simple shapes of the inclusion, since usually analytical solution of the strain or stress fields for one inclusion is needed.

From a design perspective, we need such a model that directly takes statistical information into account and doesn't depend on the size of RVE, like traditional micromechanics models. More importantly, the model can consider more than just volume fraction, but also other descriptors like inclusion shape and spatial distribution. In this paper, such a model is developed under the micromechanics style, and it will provide more accurate and general predictions on the effective properties of heterogeneous materials than traditional ones.

3. Image-based modeling techniques

The microstructure in the material should be determined before the analysis. Using high-resolution image techniques, such as SEM, TEM, LEAP and X-ray diffraction, the geometry of the microstructure can be extracted from first-hand microscopic images. The material can be characterized to distinguish between different microstructures using statistical descriptors, and have quantitative measures of the morphology. For the purpose of design, we also need to reduce the design space of the microstructure to a set of several statistical descriptors which can be optimized. From these descriptors the corresponding microstructure can be reconstructed as the solution to an inverse problem.

The majority of methods for determining the effective mechanical properties of heterogeneous materials can be classified into two categories: homogenization theories [19] and sub-scale simulation of representative volume element (RVE) [20]. Homogenization theory makes use of a method called asymptotic expansion to separate the scales for media with periodic structure, and periodic boundary conditions are applied on this unit cell. The advantage of homogenization theory is that, through an analysis on the unit cell, macroscopic properties can be predicted exactly [19]. Unfortunately, homogenization theory loses its mathematical basis for general materials with random structures (such as the microstructure we will consider), because there is no replicable unit cell. In this case, the concept of RVE comes into play and works in a more statistical sense.

According to the definition of RVE (as given by Hill [20]), the RVE size should be sufficiently large to enable the RVE to be statistically representative of the heterogeneous material, and the properties of RVE

should not depend on the boundary conditions. In practice, the RVE size in the simulation is always below Hill's definition [20], so the convergences of a property with respect to the RVE size needs to be investigated and a qualified RVE size is determined when the property values converge within a given tolerance. Moreover, average material property values should be taken to eliminate the fluctuation of properties among realizations.

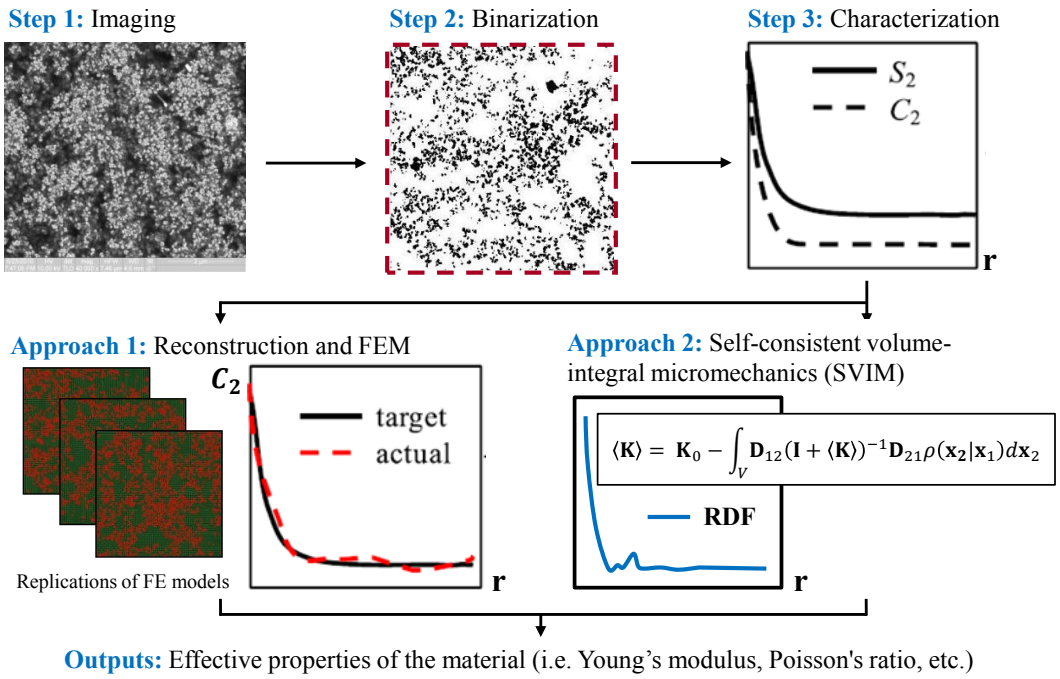

Fig. 1. The basic framework of material characterization and reconstruction for polymer composite [5, 21], as well as the micromechanics based on statistical descriptors. (r = distance between a pair of points, S_2 = two-point correlation, C_2 = two-point cluster correlation, RDF = radial distribution function. "target" refers to the desired correlation function while "actual" refers to the one of reconstructed RVE.) Figures reproduced with permission from [5].

A basic framework of the material characterization and reconstruction for a polymer composite is shown in Fig. 1 [5, 21]. In Steps 1 and 2, the original image is taken by SEM and binarized to separate the two phases. Step 3 uses the two-point correlation S_2 (the probability of finding two points in the same phase) and two-point cluster correlation C_2 (the probability of finding two points in the same cluster) to characterize the morphology of microstructures. In Step 4 (Approach 1), several realizations of the RVE whose correlation functions match the target are reconstructed and the properties of the RVEs are predicted by FEM [21]. Through the average among different RVEs, the effective properties of the material are returned

Although DNS using FEM (Approach 1) can provide accurate prediction of properties for a certain RVE, the computational cost of the simulation increases dramatically with size and complexity of the RVE due to increase in the number of elements needed. For illustration purpose, we performed the 3D viscoelastic analysis of the polymer composite with mesh size 40x40x40, 60x60x60 and 80x80x80. As shown in Fig. 2, the simulation with 80x80x80 mesh took 13.6 hours (consider at 50 frequencies), which is prohibitively long from a design perspective.

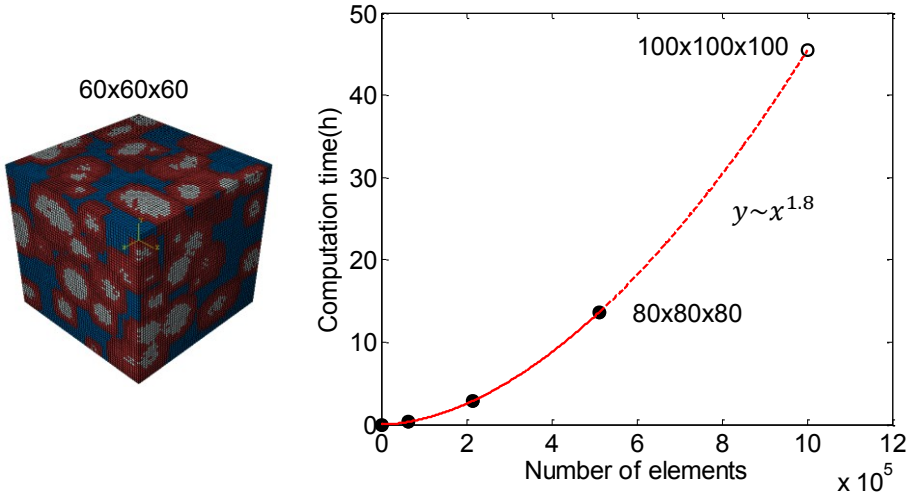

Fig. 2. Illustration of the 60x60x60 finite element mesh for the polymer composite (left) and the computational time with respect to the number of elements (right). A power law is fit to the data, and the simulation with 100x100x100 mesh is approximated to take 46 h.

In this paper, we will investigate Approach 2 as shown in Fig. 1. RVEs with different statistics are generated randomly and then these "virtual materials" are put into material characterization programs to determine the statistical descriptors, such as volume fractions and radial distribution functions. The procedure is similar to one for the real material which starts from an actual imaging processing. Then the statistical information is coupled in to a newly developed self-consistent volume-integral micromechanics model (SVIM). The SVIM's capability of predicting effective elastic properties, such as Young's modulus and Poisson's ratio, will be verified by FEA. The nearest inclusion distance and volume fraction effects shown in FEA will also be captured by SVIM. In the end, SVIM is performed to predict the effective properties of materials with different inclusion shapes.

4. Proposed self-consistent volume-integral micromechanics with statistical descriptors

In this section, we aim to obtain a macroscopic effective constitutive equation by solving a self-consistent system for multiple inclusions, rather than conducting a full direct numerical simulation at the microscale. A RVE is defined to include two phases of constituents: matrix phase with stiffness tensor $\mathbf{C}$ and inclusion phase with stiffness tensor $\mathbf{C}_\mathrm{I}$. According to the Hill-Mandel principle of macro-homogeneity [15], the RVE size should be large enough so that

$$\langle \boldsymbol{\sigma} : \boldsymbol{\varepsilon} \rangle_V = \langle \boldsymbol{\sigma} \rangle_V : \langle \boldsymbol{\varepsilon} \rangle_V, \tag{1}$$

where ":" denotes the tensor contraction, and $\langle ... \rangle_V$ is the volume averaging operator inside the RVE domain V. If Eq. (1) is satisfied, the effective constitutive relationship can be further defined as a linear form,

$$\langle \boldsymbol{\sigma} \rangle_V = \bar{\mathbf{C}} : \langle \boldsymbol{\varepsilon} \rangle_V. \tag{2}$$

where $\bar{\mathbf{C}}$ is the effective stiffness tensor. Different homogenization techniques can be used to calculate the effective modulus. In FEM, as well as FFT-based method, RVE is explicitly defined and the effective properties can be computed by solving the whole system. In contrast, traditional micromechanics methods like self-consistent and Mori-Tanaka methods don't work with an explicit RVE, but directly utilize the material properties, inclusions shapes and volume fractions of the phases to do the homogenization. Since the RVE averaging is based on the solution for one inclusion, traditional micromechanics is always much faster than the DNS simulation, but with loss of accuracy.

In this section, we will first discuss the Mori-Tanaka method which takes into account the effects of a finite RVE. However, Mori-Tanaka doesn't consider the interactions between inclusions, and that's why it always underestimates the effective modulus when the inclusion is stiffer than the matrix as shown in Section 6. On the other hand, Mori-Tanaka method can only deal with some regular inclusion shapes (e.g., circular and elliptical in 2D). In order to consider interactions and complex inclusion geometry, we propose a self-consistent volume-integral micromechanics method, which returns the effective Eshelby's tensor for arbitrary shaped inclusion and further gives the effective stiffness tensor $\bar{\mathbf{C}}$ under Mori-Tanaka averaging scheme.

4.1 Mori-Tanaka averaging scheme

In most of the micromechanics theories, the disturbances of strain field due to the appearance of inhomogeneities are given with respect to the predefined far field strain in an infinite homogeneous space. In real situation, an RVE is always finite. If we just simply define a far field strain for the finite-sized RVE, both of the strain and stress boundary conditions cannot be satisfied on ∂V [22]. In Mori-Tanaka averaging scheme, the image stress and strain are introduced to consider the effect of finite RVE,

$$\boldsymbol{\varepsilon} = \boldsymbol{\varepsilon}^0 + \boldsymbol{\varepsilon}^{pt} + \boldsymbol{\varepsilon}^{im}, \qquad \boldsymbol{\sigma} = \boldsymbol{\sigma}^0 + \boldsymbol{\sigma}^{pt} + \boldsymbol{\sigma}^{im}. \tag{3}$$

Where $\boldsymbol{\varepsilon}^0$ and $\boldsymbol{\varepsilon}^{pt}$ are the far field strain and disturbance strain due to the inhomogeneities in an infinite space, and $\boldsymbol{\varepsilon}^{im}$ is the so-called image strain due to the finite RVE, so as for the definitions of stress.

Suppose that there are many inhomogeneities in the RVE, the average stain field in the matrix can be written as $\langle\boldsymbol{\varepsilon}\rangle_M$, where $\langle ... \rangle_M$ is the volume averaging operator in the matrix. Now we can add another inhomogeneity into the RVE, then the new average strain field in the matrix is

$$\langle\boldsymbol{\varepsilon}^{new}\rangle_M = \langle\boldsymbol{\varepsilon}\rangle_M + \langle\boldsymbol{\varepsilon}^{pt}\rangle_M + \langle\boldsymbol{\varepsilon}^{im}\rangle_M. \tag{4}$$

According to the Tanaka-Mori lemma [23], we have the volume integral of disturbance strain in the matrix equal to zero, $\langle\boldsymbol{\varepsilon}^{pt}\rangle_M = \mathbf{0}$. In Mori-Tanaka method, it assumes that the average image strain due to the new inclusion can be neglected since there have already been so many inclusions in the old system, so that we also have $\langle\boldsymbol{\varepsilon}^{im}\rangle_M = \mathbf{0}$. As a result, the average strain field in the matrix remains the same,

$$\langle\boldsymbol{\varepsilon}^{new}\rangle_M = \langle\boldsymbol{\varepsilon}\rangle_M. \tag{5}$$

In the inclusion, Mori and Tanaka also set the new image strain to zero due to the same scenario, then the average strain filed in the new inclusion is expressed as

$$\langle\boldsymbol{\varepsilon}\rangle_\Omega = \langle\boldsymbol{\varepsilon}\rangle_M + \langle\boldsymbol{\varepsilon}^{pt}\rangle_\Omega. \tag{6}$$

where $\langle ... \rangle_\Omega$ is the volume averaging operator in the inclusion, and $\langle\boldsymbol{\varepsilon}^{pt}\rangle_\Omega$ is the average disturbance strain in the inclusion with respect to the average strain in the matrix, which now is regarded as the far field strain for the inclusion. Once the relationship between $\langle\boldsymbol{\varepsilon}^{pt}\rangle_\Omega$ and $\langle\boldsymbol{\varepsilon}\rangle_M$ is established, the effective stiffness can be easily calculated.

Mori and Tanaka use the Eshelby's single inclusion solution to approximate the relationship. Based on Eshelby's equivalent principle and the constant Eshelby's tensors for regular inclusions (e.g., circular and elliptical in 2D, spherical and ellipsoidal in 3D) [14], we have

$$\mathbf{C_I}\colon(\langle\boldsymbol{\varepsilon}\rangle_M + \langle\boldsymbol{\varepsilon}^{pt}\rangle_\Omega) = \mathbf{C}\colon(\langle\boldsymbol{\varepsilon}\rangle_M + \langle\boldsymbol{\varepsilon}^{pt}\rangle_\Omega - \mathbf{S}^{-1}\colon\langle\boldsymbol{\varepsilon}^{pt}\rangle_\Omega). \tag{7}$$

where $\mathbf{S}$ is the well-known Eshelby's tensor, which is basically a volume integral of Green's function of an infinite homogeneous matrix material. Then the average strain in the inclusion can be written as a function of the average strain in matrix,

$$\langle \boldsymbol{\varepsilon} \rangle_{\Omega} = -\mathbf{A} : (-\mathbf{A} - \mathbf{S})^{-1} : \langle \boldsymbol{\varepsilon} \rangle_{M}. \tag{8}$$

with the concentration factor

$$\mathbf{A} = (\mathbf{C}_{\mathrm{I}} - \mathbf{C})^{-1} : \mathbf{C}. \tag{9}$$

After the some derivations, the effective stiffness of the heterogeneous material can be expressed by

$$\bar{\mathbf{C}} = \mathbf{C}_0\{\mathbf{I} + f[\mathbf{A} + (1-f)\mathbf{S}]^{-1}\}, \tag{10}$$

where **I** is the 4th order identity tensor, and f is the volume fraction of the inclusion phase. In Mori-Tanaka averaging scheme, the average strain in the matrix is regarded as the far field strain and Eshelby's solution for one single inclusion is used. However, when the new inclusion is added into the RVE, the surrounding inclusions will interact with it, so that the strain is no longer uniformly distributed in the inclusion and Eshelby's solution doesn't work for this case. Moreover, analytical expression of Eshelby's tensor only exists for some regular geometry, so that the traditional Mori-Tanaka method cannot be applied to arbitrary inclusion shape.

In this paper, we will start from the volume integral equation [24] and discretize the inclusion domain into several integration elements. By using standard Gaussian quadrature with special polar coordinate transformation, we can calculate the self-interaction matrix **K** and pair-interaction matrix **D** for the nodal displacements. Since now the inclusion domain is discretized, arbitrary inclusion shape can be considered. Then we will introduce a self-consistent scheme which directly take the space distribution and volume fraction of inclusions into the model and outputs the effective self-interaction matrix $\langle \mathbf{K} \rangle$. Based on $\langle \mathbf{K} \rangle$, the effective Eshelby's tensor $\bar{\mathbf{S}}$ can be computed. Similar to Eq. (10), the effective stiffness of the material is

$$\bar{\mathbf{C}} = \mathbf{C}_0\{\mathbf{I} + f[\mathbf{A} + (1-f)\bar{\mathbf{S}}]^{-1}\}, \tag{11}$$

4.2 Volume integral method

For an elastostaic problem of heterogeneous material, the governing equation in partial differential form is equivalent to a volume integral equation [24],

$$u_m(\mathbf{x}) = u_m^0(\mathbf{x}) - \int_R \delta C_{ijkl}(\boldsymbol{\xi})\, g_{i,j}^m(\boldsymbol{\xi}, \mathbf{x}) u_{k,l}(\boldsymbol{\xi}) d\boldsymbol{\xi}, \tag{12}$$

where $u_m(\mathbf{x})$ is the m-th component of the displacement at point **x**, and $u_m^0(\mathbf{x})$ is the m-th component of the far field displacement without the appearance of the inhomogeneities. $\delta C_{ijkl}(\boldsymbol{\xi})$ is the difference of stiffness tensor between the inhomogeneities and matrix at point $\boldsymbol{\xi}$, which is $\delta C_{ijkl}(\boldsymbol{\xi}) = C_{ijkl}^I(\boldsymbol{\xi}) - C_{ijkl}$, so that the integral is only nonzero in the inclusion phases. $g_i^m(\boldsymbol{\xi}, \mathbf{x})$ is the static Green's function of Navier's equation in an infinite space, which represents the i-th component of the displacement at point $\boldsymbol{\xi}$ due to the force at point **x**. Green's functions and their derivatives of 2D plane strain and 3D isotropic material are provided in the Appendix. The integral is over the whole domain. As we can see from Eq. (12), the disturbances of the displacement from different inclusions can be superimposed.

For the simplicity of demonstration, let's consider a system with two non-overlapping inclusions with arbitrary shapes, as illustrated in Fig. 3. Then the volume integral equation for the displacement equation in the first equation becomes,

$$u_m^1(\mathbf{x}) = u_m^{01}(\mathbf{x}) - \int_{\Omega_1} \delta C_{ijkl}(\boldsymbol{\xi})\, g_{i,j}^m(\boldsymbol{\xi}, \mathbf{x}) u_{k,l}^1(\boldsymbol{\xi}) d\boldsymbol{\xi} - \int_{\Omega_2} \delta C_{ijkl}(\boldsymbol{\xi})\, g_{i,j}^m(\boldsymbol{\xi}, \mathbf{x}) u_{k,l}^2(\boldsymbol{\xi}) d\boldsymbol{\xi}. \tag{13}$$

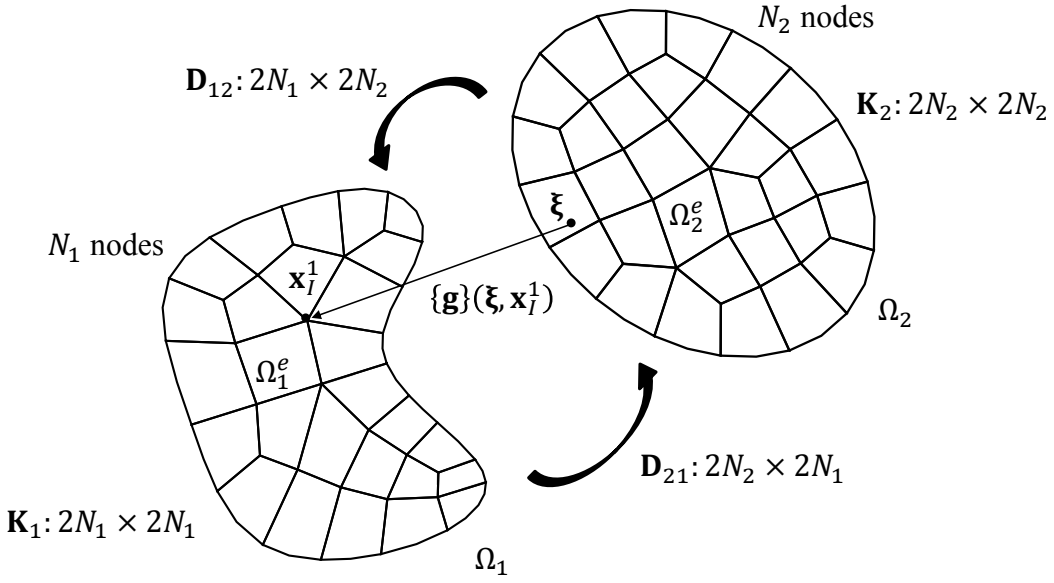

Fig. 3. Illustration of volume integral method for two inclusions in 2D, and dimensions of the interaction matrices K and D. N_1 and N_2 are the numbers of nodes in the first and second inclusion, {g} is the Green's function at nodal point.

The first integral on the R.H.S. represents self-influence of displacements in the first inclusion, while the second integral represents in the influence of displacement in the second inclusion on the displacement in the first inclusion. Due to the symmetry of the stiffness tensor, we can further simplify the equation using Voigt notation,

$$\int_{\Omega_1} \delta C_{ijkl}(\boldsymbol{\xi})\, g_{i,j}^m(\boldsymbol{\xi}, \mathbf{x}) u_{k,l}^1(\boldsymbol{\xi}) d\boldsymbol{\xi} \to \int_{\Omega_1} \{\mathbf{g}\}_I^m(\boldsymbol{\xi}, \mathbf{x}) \{\delta \mathbf{C}\}_{IJ}(\boldsymbol{\xi}) \{\boldsymbol{\varepsilon}^1\}_J(\boldsymbol{\xi}) d\boldsymbol{\xi}. \tag{14}$$

The strain in each element can be approximated by the standard FEM shape functions,

$$\{\boldsymbol{\varepsilon}^1\} = [\varepsilon_{11}^1, \quad \varepsilon_{22}^1, \quad \varepsilon_{12}^1 + \varepsilon_{21}^1]^T = \mathbf{B}\{\mathbf{u}^1\}. \tag{15}$$

where $\{\mathbf{u}^1\} = \mathbf{U}^1$ is the Voigt notation of displacements for all the discretized nodes in the first inclusion. In general, $\{...\}$ denotes the Voigt notation. Define the Green's function at nodal points $\mathbf{x} = \mathbf{x}_I^1$ of the first inclusion

$$\mathbf{G}_I^1(\boldsymbol{\xi}) =. \{\mathbf{g}\}(\boldsymbol{\xi}, \mathbf{x}_I^1) \tag{16}$$

Extract the nodal displacement from the integral, Eq. (13) can be rewritten in Voigt notation,

$$\mathbf{U}^1 = \mathbf{U}_1^0 - \left(\int_{\Omega_1} \mathbf{G}^1 \{\delta \mathbf{C}\} \mathbf{B} d\boldsymbol{\xi} \right) \mathbf{U}^1 - \left(\int_{\Omega_2} \mathbf{G}^1 \{\delta \mathbf{C}\} \mathbf{B} d\boldsymbol{\xi} \right) \mathbf{U}^2, \tag{17}$$

which is now a system of linear equations. Define

$$\mathbf{K}_1 = \int_{\Omega_1} \mathbf{G}^1 \{\delta \mathbf{C}\} \mathbf{B} d\boldsymbol{\xi}, \qquad \mathbf{D}_{12} = \int_{\Omega_2} \mathbf{G}^1 \{\delta \mathbf{C}\} \mathbf{B} d\boldsymbol{\xi}, \tag{18}$$

where $\mathbf{K}_1$ is the self-interaction matrix of the first inclusion, while $\mathbf{D}_{21}$ is the pair-interaction matrix indicating effect of displacement in the second inclusion on that in the first inclusion. For a 2D problem, if 4-node bilinear element is used for the discretization and two inclusions have N_1 and N_2 nodes inside, the sizes of $\mathbf{G}_e^1$, $\{\delta \mathbf{C}\}$, $\mathbf{B}_e$ in each integration element are $2N_1 \times 3, 3 \times 3$ and 3×8 respectively. After

assembling of elementary matrices, the sizes of global interaction matrix $\mathbf{K}_1$ and $\mathbf{D}_{21}$ are $2N_1 \times 2N_1$ and $2N_1 \times 2N_2$ respectively.

It should be noted that evaluation of singular integral involved in the expression of the self-interaction matrix $\mathbf{K}_1$, when the integration point is exactly at one of the nodal points within the first inclusion. As we can see from the expressions of the Green's functions, $\mathbf{G}^1$ has an r^{-1} singularity around the nodal points in 2D, and r^{-2} singularity in 3D. Unfortunately, standard numerical integration loses its accuracy when singularity appears in the integral. As recommended in [25], a special polar coordinate transformation based on triangle (2D) or tetrahedron (3D) polar coordinates is introduced to get rid of the singularity. After the transformation, we can evaluate the new integrals using standard Gaussian quadrature efficiently.

Similar to Eq. (17), the system of equations of nodal displacements for *N* non-overlapping inclusions can be written generally as,

$$\mathbf{U}^n = \mathbf{U}_n^0 - \mathbf{K}_n\mathbf{U}^n - \sum_{i=1, i\neq n}^{N} \mathbf{D}_{ni}\mathbf{U}^i, n = 1, 2, \dots N, \tag{19}$$

where $\mathbf{U}^n$ is the nodal displacement in the *n*-th inclusion, and $\mathbf{U}_n^0$ is the far field displacement for the original homogeneous matrix material. $\mathbf{K}_n$ is the self-interaction matrix of the *n*-th inclusion, and $\mathbf{D}_{ni}$ is the pair-interaction matrix representing the portion of nodal displacement in the *n*-th inclusion resulting from the nodal displacement in the *i*-th inclusion. Equivalent to Eq. (19), the system of equations for N inclusion can be also written in matrix form,

$$\begin{bmatrix} \mathbf{U}^1 \\ \mathbf{U}^2 \\ \vdots \\ \mathbf{U}^N \end{bmatrix} = [\mathbf{K}]^{-1} \begin{bmatrix} \mathbf{U}_1^0 \\ \mathbf{U}_2^0 \\ \vdots \\ \mathbf{U}_N^0 \end{bmatrix} \tag{20}$$

with

$$[\mathbf{K}] = \begin{bmatrix} \mathbf{I} + \mathbf{K}_1 & \mathbf{D}_{12} & \cdots & \mathbf{D}_{1N} \\ \mathbf{D}_{21} & \mathbf{I} + \mathbf{K}_2 & \cdots & \mathbf{D}_{2N} \\ \vdots & & \ddots & \vdots \\ \mathbf{D}_{N1} & \mathbf{D}_{N2} & \cdots & \mathbf{I} + \mathbf{K}_N \end{bmatrix}. \tag{21}$$

Suppose there are in total *M* discretized nodes of all the inclusions, then the dimensions of $[\mathbf{K}]$ are $2M \times 2M$ and $3M \times 3M$ in 2D and 3D respectively.

4.3 Newly developed self-consistent scheme

Although the nodal displacements in each inclusion can be obtained directly by solving Eq. (20) for any realization of a random material, it is time-consuming in terms of the numerical integration of the self-interaction and pair-interaction matrices for each inclusion, and each set of results only corresponds to a certain realization of the microstructure. As mentioned before, the real RVE is also finite which means that we need to find either the appropriate far field displacement, or the Green's function for a finite domain. On the other hand, we are more interested in the averaged displacement in all the inclusions and the effective properties, rather than the displacement at every point in the domain. Rather than reconstructing the RVE and performing DNS analysis, we will introduce a self-consistent scheme which directly takes the inclusion shape, volume fraction and radial distribution function into the model and

outputs the ensemble-averaged displacement in the inclusion, as well as the overall effective stiffness tensor.

Let us start from Eq. (20) for system with N inclusions. The next step is to insert another inclusion into the original RVE without overlapping with previous inclusions. Due to the appearance of the $(N+1)$-th inclusion, the displacements in the previous N inclusions are perturbed with respect to the original field, the resulting system of the linearized volume integral equations for N inclusions is,

$$\begin{bmatrix} \mathbf{U}^1 + \Delta\mathbf{U}^1 \\ \mathbf{U}^2 + \Delta\mathbf{U}^2 \\ \vdots \\ \mathbf{U}^N + \Delta\mathbf{U}^N \end{bmatrix} = [\mathbf{K}]^{-1} \begin{bmatrix} \mathbf{U}_1^0 - \mathbf{D}_{1(N+1)}\mathbf{U}^{N+1} \\ \mathbf{U}_2^0 - \mathbf{D}_{2(N+1)}\mathbf{U}^{N+1} \\ \vdots \\ \mathbf{U}_N^0 - \mathbf{D}_{N(N+1)}\mathbf{U}^{N+1} \end{bmatrix}, \tag{22}$$

where $\Delta\mathbf{U}^i$ is the change of nodal displacements in the i-th inclusion after inserting the $(N+1)$-th inclusion into the matrix. Subtracting Eq. (20) from Eq. (22), gives a modified set of linear algebraic equations for $\Delta\mathbf{U}^i$,

$$\begin{bmatrix} \Delta\mathbf{U}^1 \\ \Delta\mathbf{U}^2 \\ \vdots \\ \Delta\mathbf{U}^N \end{bmatrix} = [\mathbf{K}]^{-1} \begin{bmatrix} \mathbf{D}_{1(N+1)} \\ \mathbf{D}_{2(N+1)} \\ \vdots \\ \mathbf{D}_{N(N+1)} \end{bmatrix} \mathbf{U}^{N+1}. \tag{23}$$

Furthermore, with all the information from the N inclusions, the volume integral equation of the $(N+1)$-th inclusion can be written as

$$\mathbf{U}^{N+1} = \mathbf{U}_{N+1}^0 - \mathbf{K}_{N+1}\mathbf{U}^{N+1} - \begin{bmatrix} \mathbf{D}_{1(N+1)} & \mathbf{D}_{1(N+1)} \cdots \mathbf{D}_{1(N+1)} \end{bmatrix} \begin{bmatrix} \mathbf{U}^1 + \Delta\mathbf{U}^1 \\ \mathbf{U}^2 + \Delta\mathbf{U}^2 \\ \vdots \\ \mathbf{U}^N + \Delta\mathbf{U}^N \end{bmatrix}, \tag{24}$$

substituting Eq. (22) into Eq. (24) gives

$$\begin{aligned} \mathbf{U}^{N+1} = \mathbf{U}_{N+1}^0 - \mathbf{K}_{N+1}\mathbf{U}^{N+1} - \begin{bmatrix} \mathbf{D}_{1(N+1)} & \mathbf{D}_{1(N+1)} \cdots \mathbf{D}_{1(N+1)} \end{bmatrix} \begin{bmatrix} \mathbf{U}^1 \\ \mathbf{U}^2 \\ \vdots \\ \mathbf{U}^N \end{bmatrix} \\ + \begin{bmatrix} \mathbf{D}_{1(N+1)} & \mathbf{D}_{1(N+1)} \cdots \mathbf{D}_{1(N+1)} \end{bmatrix} [\mathbf{K}]^{-1} \begin{bmatrix} \mathbf{D}_{1(N+1)} \\ \mathbf{D}_{2(N+1)} \\ \vdots \\ \mathbf{D}_{N(N+1)} \end{bmatrix} \mathbf{U}^{N+1}, \end{aligned} \tag{25}$$

Eq. (25) works for general cases with arbitrary microstructures. Now we will make the assumption that all the inclusions have the same shape, discretization mesh and material properties. If the inclusions are unidirectional aligned, we further assume all the inclusion have the same ensemble-averaged displacement $\langle\mathbf{U}\rangle$, so that $\langle\mathbf{U}^i\rangle = \langle\mathbf{U}\rangle$. We can define the effective self-interaction matrix $\langle\mathbf{K}\rangle$ (which includes the interaction between inclusions) by

$$\langle\mathbf{U}\rangle = \mathbf{U}^0 - \langle\mathbf{K}\rangle\langle\mathbf{U}\rangle. \tag{26}$$

After taking the ensemble average of Eq. (20), we have

$$\langle[\mathbf{K}]\rangle = \begin{bmatrix} (\mathbf{I}+\langle\mathbf{K}\rangle)^{-1} & \cdots & \mathbf{0} \\ \vdots & \ddots & \vdots \\ \mathbf{0} & \cdots & (\mathbf{I}+\langle\mathbf{K}\rangle)^{-1} \end{bmatrix}. \tag{27}$$

Since the inclusions are randomly distributed, we can assume the ensemble averaged values $\langle\mathbf{U}\rangle$ and $\langle[\mathbf{K}]\rangle$ of the previous N inclusions don't correlate to the *(N+1)*-th inclusion. After taking the ensemble average of Eq. (25), we can derive

$$\langle\mathbf{U}\rangle = \mathbf{U}^0 - \mathbf{K}_0\langle\mathbf{U}\rangle - \left(\int_V \mathbf{D}_{12}\rho(\mathbf{x_2}|\mathbf{x}_1)d\mathbf{x}_2\right)\langle\mathbf{U}\rangle + \left(\int_V \mathbf{D}_{12}(\mathbf{I}+\langle\mathbf{K}\rangle)^{-1}\mathbf{D}_{21}\rho(\mathbf{x_2}|\mathbf{x}_1)d\mathbf{x}_2\right)\langle\mathbf{U}\rangle, \tag{28}$$

where $\rho(\mathbf{x_2}|\mathbf{x_1})$ is the conditional number density of the surrounding inclusion at point $\mathbf{x}_2$ given the first inclusion locate at point $\mathbf{x}_1$, representing the distribution of the inclusions and serving as statistical descriptors of the microstructure. $\mathbf{K}_0$ is the original self-interaction matrix of the inclusion. Due to the symmetry of pair-interaction matrix, the third term on the R.H.S. of Eq. (28) vanishes,

$$\int_V \mathbf{D}_{12}\rho(\mathbf{x_2}|\mathbf{x}_1)d\mathbf{x}_2 = 0, \tag{29}$$

Then by comparing Eq. (28) to Eq. (26), we reach the self-consistent equation,

$$\langle\mathbf{K}\rangle = \mathbf{K}_0 - \int_V \mathbf{D}_{12}(\mathbf{I}+\langle\mathbf{K}\rangle)^{-1}\mathbf{D}_{21}\rho(\mathbf{x_2}|\mathbf{x}_1)d\mathbf{x}_2, \tag{30}$$

The self-consistent equation can be solved iteratively as we will discuss in Section 4.4. In fact, the effective self-interaction matrix $\langle\mathbf{K}\rangle$ indicates the relationship between effective strain in the inclusion and far field strain, with consideration of inclusion interactions. The far field displacement $\mathbf{U}^0$ is a linear function of far field strain $\boldsymbol{\varepsilon}^0$,

$$\mathbf{U}^0 = \mathbf{F}\{\boldsymbol{\varepsilon}^0\}, \tag{31}$$

where $\mathbf{F}$ is a function of the nodal coordinates of the inclusion. If there are N_0 nodes in the inclusion, the size of $\mathbf{F}$ is $2N_0 \times 3$ and $3N_0 \times 6$ in 2D and 3D. Then the average strain in the inclusion can be calculated using the shape functions,

$$\{\langle\boldsymbol{\varepsilon}\rangle_\Omega\} = \int_\Omega \mathbf{B}\langle\mathbf{U}\rangle d\mathbf{x} = \left(\int_\Omega \mathbf{B}d\mathbf{x}\,(\mathbf{I}+\langle\mathbf{K}\rangle)^{-1}\mathbf{F}\right)\{\boldsymbol{\varepsilon}^0\}. \tag{32}$$

According to the Eshelby's equivalent principle, the effective Eshelby's tensor of the inclusion is,

$$\bar{\mathbf{S}} = \left(\int_\Omega \mathbf{B}(\mathbf{I}+\langle\mathbf{K}\rangle)^{-1}d\mathbf{x}\,\mathbf{F}\right)^{-1}\{\mathbf{A}\} - \{\mathbf{A}\}. \tag{33}$$

where $\{\mathbf{A}\}$ is the concentration factor under Voigt notation as defined in Section 4.1. Then we can calculate the effective stiffness tensor using Eq. (11). More generally, if the inclusions are randomly oriented, we also need to average over all the possible orientations of the surrounding inclusions. Suppose θ represents the rotation of the inclusion, and the modified effective self-interaction matrix under the rotation is

$$\langle\mathbf{K}_\theta\rangle = \mathbf{R}_\mathrm{u}(\theta)^{-1}\langle\mathbf{K}\rangle\mathbf{R}_\mathrm{u}(\theta), \tag{34}$$

where $\mathbf{R}_\mathrm{u}(\theta)$ is the transformation matrix of displacements under the rotation of coordinate system, and we have $\mathbf{R}_\mathrm{u}^T\mathbf{R}_\mathrm{u} = \mathbf{I}$. Moreover, the modified effective Eshelby's tensor can be expressed as,

$$\bar{\mathbf{S}} = \left(\langle \mathbf{R}_\varepsilon(\theta)^{-1} \left(\int_\Omega \mathbf{B}(\mathbf{I} + \langle \mathbf{K} \rangle)^{-1} d\mathbf{x}\, \mathbf{F} \right) \mathbf{R}_\varepsilon(\theta) \rangle_\theta \right)^{-1} \{\mathbf{A}\} - \{\mathbf{A}\}, \tag{35}$$

where $\mathbf{R}_\varepsilon(\theta)$ is the transformation matrix of strain under the rotation of coordinate system, and $\langle \dots \rangle_\theta$ denotes the average operator over inclusions' orientation.

4.4 Self-consistent equation

In self-consistent equation, $\rho(\mathbf{x_2}|\mathbf{x_1})$ is the conditional number density function. As mentioned in Section 4.3, it is determined by the microstructures in the material, which strongly depends on the volume fraction of the inhomogeneities (or secondary phases) and the distance between the two inhomogeneities given by the position $\boldsymbol{r} = |\mathbf{x}_2 - \mathbf{x}_1|$. In this paper, we will describe the microstructure by the radial distribution function (RDF) $g(r)$, and the conditional number density of the surrounding particles $\rho(\mathbf{x_2}|\mathbf{x_1})$ can be expressed as

$$\rho(\mathbf{x_2}|\mathbf{x_1}) = \frac{N}{V} g(r). \tag{36}$$

Radial distribution functions are well studied theoretically in statistical mechanics [26]. For example, the Ornstein-Zernike direct correlation function together with the Percus-Yevick assumption solution for hard spheres leads to excellent approximation of radial distribution function $g(r)$ even at high particle volume fractions [27].

On an atomic scale, the radial distribution function can also be determined experimentally using neutron scattering or x-ray scattering and measuring the structure factor which directly relates to the radial distribution function. In our case, optical methods like SEM and TEM are used to determine RDF as well as to reveal the morphology of the microstructure. For instance, by marking the center point of each fiber in a 2D SEM image of fiber reinforced polymer composite, we can use the coordinates of the center points to calculate the radial distribution function for fiber composite.

Eq. (30) is a nonlinear equation for $\langle \mathbf{K} \rangle$ which explicitly depends on the distribution of the inclusions in the RVE which can be described by RDF, and an iteration scheme is used to solve the nonlinear equation. This iteration scheme determines a new $\langle \mathbf{K} \rangle$ by substituting a previous value of $\langle \mathbf{K} \rangle$ into the equation and step forward by a step factor α until the norm of the difference is below a certain tolerance.

1) Set index $p = 1$, $\langle \mathbf{K} \rangle^0 = \mathbf{K}_0$ and step factor α
2) Calculate $\langle \mathbf{K} \rangle'$

$$\langle \mathbf{K} \rangle' = \mathbf{K}_0 - \int_V \mathbf{D}_{12} (\mathbf{I} + \langle \mathbf{K} \rangle^{p-1})^{-1} \mathbf{D}_{21} \rho(\mathbf{x_2}|\mathbf{x_1}) d\mathbf{x}_2, \tag{37}$$

3) Step forward to $\langle \mathbf{K} \rangle^p$

$$\langle \mathbf{K} \rangle^p = \langle \mathbf{K} \rangle^{p-1} + (1 + \alpha)(\langle \mathbf{K} \rangle' - \langle \mathbf{K} \rangle^{p-1}), \tag{38}$$

4) If $\|\langle \mathbf{K} \rangle^p - \langle \mathbf{K} \rangle^{p-1}\| < tolerance$ then

$$\langle \mathbf{K} \rangle = \langle \mathbf{K} \rangle^p$$

   Endif

5) $p = p + 1$
6) Go to Step 2

In Section 6.1, we will show how the step factor influence the convergence of the iteration scheme. After obtaining $\langle \mathbf{K} \rangle$, the effective Eshelby's tensor and effective stiffness tensor can be calculated under Mori-Tanaka averaging scheme.

5. Implementation

To demonstrate the method, we will restrict the analysis to 2D plane strain and 3D problems for a two-phase linear elastic material, and to rectangular and cubic RVEs containing randomly dispersed identical non-overlapping inhomogeneities. For 2D plane strain problems, an algorithm based on two specially developed techniques for moving inclusions is used for generating the RVE for high values of volume fraction, and the nearest inclusion distance (NID) can be explicitly specified in the program [28]. For 3D problems, RVEs are generated using molecular dynamics simulation and LJ potential is applied to control the distance between particles. Then geometries of the RVEs are input into finite element analysis with periodic boundary conditions. Simultaneously, the geometrical information is also used for the statistical analysis and extracting the radial distributions functions of the microstructure. By putting RDF into SVIM, we can calculate the overall effective elastic properties, such as Young's modulus and Poisson ratio.

5.1 FEA on RVEs

For the finite element (FE) modeling in 2D, RVEs are meshed by the plane strain 3-node triangle element with linear shape functions for the simplicity of mesh generation and the periodic boundary conditions are applied to the RVEs. As we can see from Fig. 4, the periodic boundary conditions force the shape of the deformed RVE to be a parallelogram and the positions of the four corners will control the overall macroscopic strain. The bottom-left corner is fixed to eliminate the rigid body motion. As a result, the right-top and right-bottom corners have independent degrees of freedom.

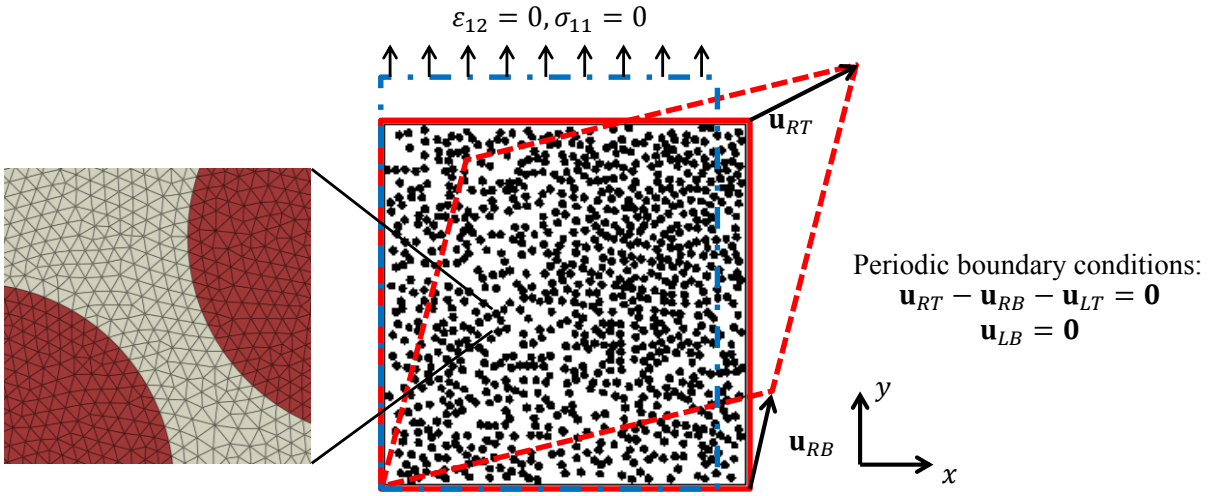

Fig. 4. Illustrations for the finite element mesh (volume fraction 30%) in 2D and the periodic boundary conditions. The dashed line represents the general case of the RVE deformation, while the dash-dotted line is the boundary conditions applied in this paper.

To simplify the computation of the overall elastic properties, we forced the boundary condition to satisfy $\varepsilon_{12} = 0$, $\sigma_{11} = 0$. In this case, the shape of the deformed RVE is still rectangular. The nodes on the left edge and bottom edge have no displacement in the x-direction and y-direction respectively. The nodes on the right edge share the same displacement in the x-direction with the top-right (RT) corner, while the nodes on the top edge share the same displacement in the y-direction. A movement in the y-direction is applied to top-right (RT) corner, and it should be stated that the value of the movement is arbitrary since the material is linear elastic.

In the FEA, the stress and strain at a numerical integration point in each element are used to calculate their average values in the RVE, as well as the overall elastic properties. Following the standard averaging procedure, the overall elastic properties can be expressed as

$$v_2 = -\frac{\sum_{i=1}^{N_e} \varepsilon_{11}^i A_i}{\sum_{i=1}^{N_e} \varepsilon_{22}^i A_i}, \qquad E_2 = \frac{\sum_{i=1}^{N_e} \sigma_{22}^i A_i}{\sum_{i=1}^{N_e} \varepsilon_{22}^i A_i}, \tag{39}$$

where v_2 and E_2 are the transverse Poisson's ratio and Young's modulus in the y direction, A_i is the area of the i-th element, and N_e is the total number of elements in the RVE.

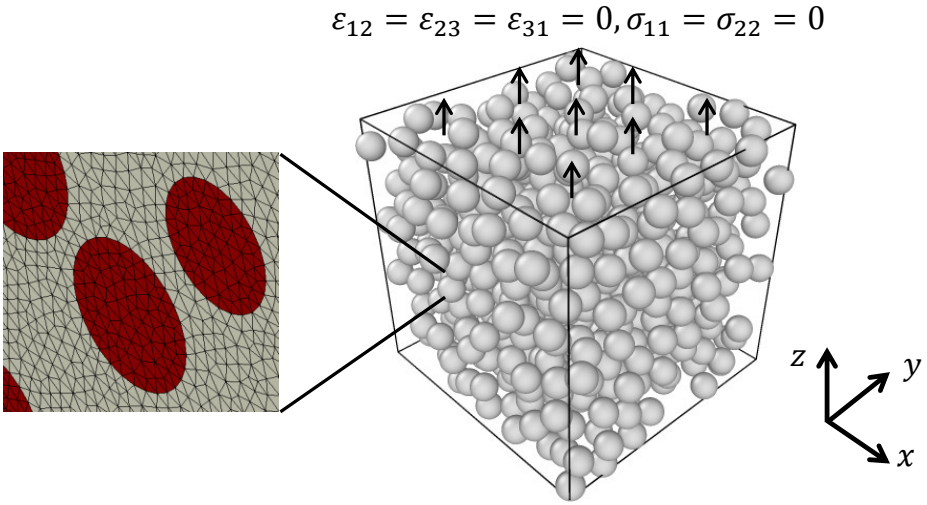

Fig. 5. Illustrations for the finite element mesh (volume fraction 30%) in 3D and the boundary conditions.

For FE modeling in 3D, RVEs are meshed using 4-node tetrahedral element. The geometry of an instance of RVE and its FE mesh are provided in Fig. 5. Similar to 2D models, the boundary conditions are $\varepsilon_{12} = \varepsilon_{23} = \varepsilon_{31} = 0$, $\sigma_{11} = \sigma_{22} = 0$. Thus, the overall elastic properties can be expressed as

$$v = -\frac{\sum_{i=1}^{N_e} \varepsilon_{11}^i V_i}{\sum_{i=1}^{N_e} \varepsilon_{33}^i V_i}, \qquad E = \frac{\sum_{i=1}^{N_e} \sigma_{33}^i V_i}{\sum_{i=1}^{N_e} \varepsilon_{33}^i V_i}, \tag{40}$$

where v and E are the Poisson's ratio and Young's modulus, V_i is the volume of the i-th element, and N_e is the total number of elements in the RVE.

5.2 Analysis using SVIM

In order to solve the self-consistent equation, we need to extract the radial distribution function from the randomly generated RVEs. In practice, we should define a cutoff distance r_{cut} which corresponds to a certain accuracy of the integration. Since the RVE is periodic, it can be replicated for the calculation of RDF. Take the analysis of 2D RVE as an example. For each inclusion in the RVE, the distance from it to all the surrounding inclusions in its integration domain are recorded and binned into a histogram and then the average is taken among all the inclusion. The number of inclusions $\Delta N(r)$ at the distance between r and $r + \Delta r$ to the center of the reference inclusions can be extracted from the microstructure, and its relationship to the RDF $g(r)$ is shown below

$$\Delta N(r) = \frac{N}{V} g(r) 2\pi r \Delta r = f \frac{2\pi \Delta r g(r)}{A_c} r, \tag{41}$$

where f is the volume fraction of the inclusion phase and A_c is the area of the inclusion, so that the RDF in 2D is,

$$g(r) = \frac{A_c}{2\pi\Delta r f}\left(\frac{\Delta N(r)}{r}\right) \text{ in } 2D. \tag{42}$$

Based on the statistical analysis on the microstructures, the integral in the self-consistent equation can be evaluated numerically in a polar coordinate system (based on a radius r and angle θ) as:

$$\begin{aligned}\int_V \mathbf{D}_{12}(\mathbf{I} + \langle \mathbf{K} \rangle^{p-1})^{-1}\mathbf{D}_{21}\rho(\mathbf{x_2}|\mathbf{x}_1)d\mathbf{x}_2 &= \int_r \int_\theta \mathbf{D}_{12}(\mathbf{I} + \langle \mathbf{K} \rangle^{p-1})^{-1}\mathbf{D}_{21}\frac{N}{V}g(r)rd\theta \mathrm{d}r \\ &= \sum\nolimits_{r=0}^{r_{cut}}\left\{\frac{1}{2\pi}\sum\nolimits_{\theta=0}^{2\pi}\mathbf{D}_{12}(\mathbf{I} + \langle \mathbf{K} \rangle^{p-1})^{-1}\mathbf{D}_{21}d\theta\right\} f\frac{2\pi g(r)r}{A_c}\Delta r \text{, in 2D.}\end{aligned} \tag{43}$$

Similarly, the RDF in 3D is,

$$g(r) = \frac{V_c}{4\pi\Delta r f}\left(\frac{\Delta N(r)}{r^2}\right) \text{ in } 3D, \tag{44}$$

where V_c is the volume of the inclusion. The integral term in 3D self-consistent equation can be rewritten as,

$$\begin{aligned}&\int_V \mathbf{D}_{12}(\mathbf{I} + \langle \mathbf{K} \rangle^{p-1})^{-1}\mathbf{D}_{21}\rho(\mathbf{x_2}|\mathbf{x}_1)d\mathbf{x}_2 \\ &\quad = \sum\nolimits_{r=0}^{r_{cut}}\left\{\frac{1}{N_s}\sum\nolimits_{i=1}^{N_s}\mathbf{D}_{12}(\mathbf{x}_i)(\mathbf{I} + \langle \mathbf{K} \rangle^{p-1})^{-1}\mathbf{D}_{21}(\mathbf{x}_i)\right\} f\frac{4\pi g(r)r^2}{V_c}\Delta r \text{ in 3D,}\end{aligned} \tag{45}$$

where $\mathbf{x}_1, \mathbf{x}_2, .., \mathbf{x}_{N_s}$ are uniformly distributed points on the sphere with radius r. The cutoff distance r_{cut} and the interval of discretization Δr are two parameters relating to the result of the integral, as well as the overall elastic properties. As $r_{cut} \to \infty$ and $\Delta r \to 0$, the convergence of the result will be reached. In order to have a balance between accuracy and efficiency, we will choose $r_{cut} = 10L$ and $\Delta r = 0.025L$ where L is the characteristic length of the inclusion.

In terms of the discretization of inclusion, higher order elements are preferred since they allow a better approximation of curved surfaces. In 2D, 8-node quadratic, quadrilateral elements are used for the meshing. With increasing distance r, the number of integration points of Gaussian quadrature in each element ranges from 6×6 to 1×1. In 3D, 20-node Quadratic, hexahedral elements are used, and the number of integration points ranges from $4 \times 4 \times 4$ to $1 \times 1 \times 1$.

6. Results and Discussion

We will first check the convergence of the elastic properties with respect to the RVE size in 2D FEA, and determine the RVE size for the following sets of simulations. Then the convergence of elastic properties with respect to step factor α in SVIM is investigated. For 2D plane strain materials with non-overlapping circular inclusions, we demonstrate the effects of volume fraction and nearest inclusion distance (NID) in FEA and SVIM. For 3D materials with non-overlapping spherical inclusions, the capability of SVIM in capturing the effect of volume fraction is validated against both experiments and FEA. Finally, we use SVIM to predict the effect of inclusion shapes on elastic properties of 2D plane strain material.

6.1 Convergence study

In the convergence studies on FEA and SVIM, the elastic properties of the matrix and inclusion materials are $E_m = 3.0$ GPa, $v_m = 0.3$, $E_c = 100$ GPa, $v = 0.3$. In FEA, a set of models with RVE size 5, 10, 20,

40 μm is generated under volume fraction 50% and NID 0.04 μm. There are 12 replications for 5, 10 and 20 μm RVEs and one replication for 40 μm RVE.

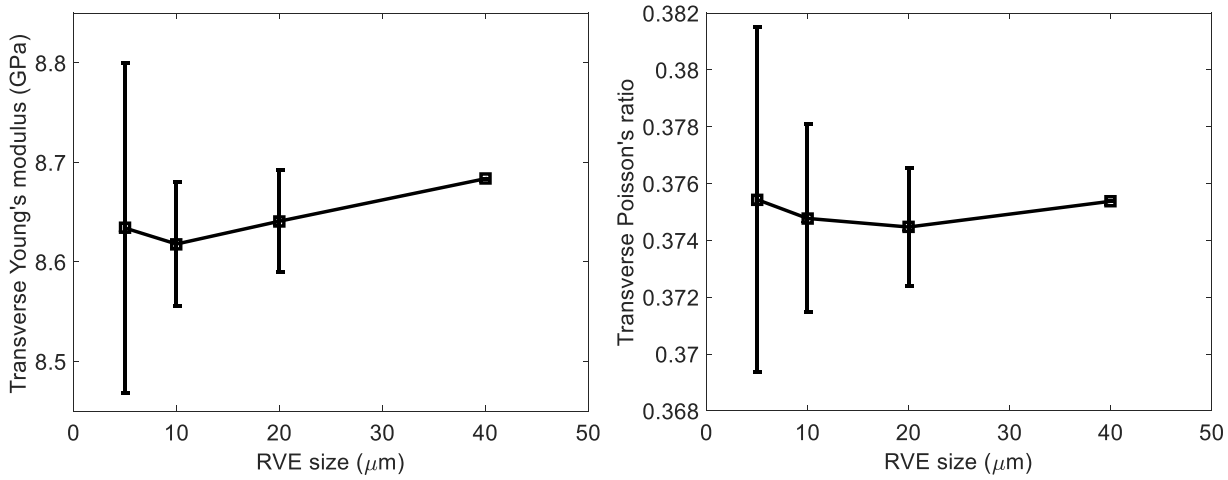

Fig. 6. Effective transverse Young's modulus and Poisson's ratio as a function of increasing RVE size.

As we can see from Fig. 6, both of the transverse Young's modulus and Poisson's ratio converge as the RVE becomes larger, and the deviation among replications also decreases at the same time. For following FEA simulations, we will use 20 μm RVE in order to avoid the meshing and memory issues in FEM of large RVEs. A typical running time of a 20 μm RVE takes approximately 15 minutes with 4 quad core 2.0 Ghz E5335 Xeon processors.

To check the convergence of SVIM, the iteration histories of transverse Young's modulus and Poisson's ratio are provided Fig. 7, and the influence of the step factor α is investigated.

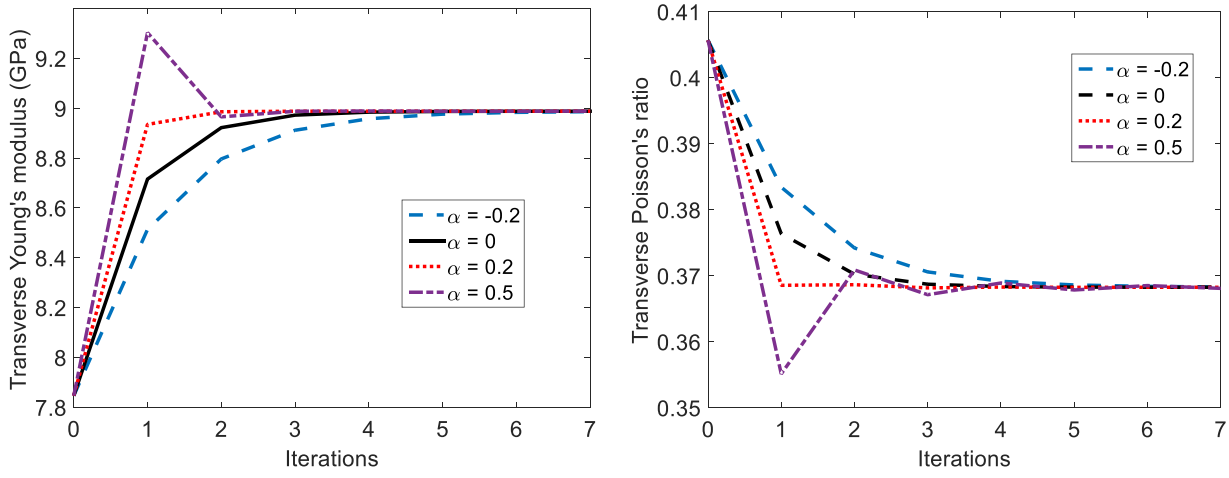

Fig. 7. Iteration histories of SVIM with different step factor α.

All the results converge within 7 iteration under a tolerance of 0.01%, however, the step factor α controls the convergence rate. When $\alpha = -0.2$, it converges slower than the original scheme without step factor. When $\alpha = 0.5$, it overshoots the converged value. It turns out 0.2 is the optimal step factor that gives us a higher convergence rate, and we will keep $\alpha = 0.2$ for all the SVIM calculations in 2D and 3D. Using

one Intel® Core™ i7 CPU, typical running times of SVIM with around 30 elements in the inclusion are approximately 1 minutes in 2D and 15 minutes in 3D. It should be noted that the running time can be reduced through parallel computing, and SVIM can be easily parallelized by distributing the integration in Eq. (37).

6.2 2D plane strain problems with circular inclusions

In this section, the elastic properties of the matrix and inclusion materials are $E_m = 3.0$ GPa, $v_m = 0.3, E_c = 100$ GPa, $v = 0.3$. The radius of the circular inclusions is equal to 0.2 μm, so that the characteristic length of the inclusion is $L = 2a = 0.4\ \mu m$. As recommended in Section 5.2, the cut-off distance r_{cut} is equal to 4 μm and the interval of discretization is equal to 0.01 μm. For all the models, the RVE size is chosen to be 20 μm, and the nearest inclusion distance varies from 0.01 to 0.19 μm which the volume fraction of the inclusions varies from 10% to 55%. In the finite element model, the average element size is 0.003 μm.

Following the procedure in Section 5.2, RDF was calculated and averaged among all the replications of each set of RVEs, and it was put into the self-consistent equation to compute the effective properties, such as the effective self-interaction matrix $\langle \mathbf{K} \rangle$. For a 2D plane strain material containing circular inclusions with volume fraction 30% and NID 0.04 μm, the effective distribution of strain ε_{22} in the inclusion under a far field strain $\{\boldsymbol{\varepsilon}^0\} = [-0.02, 0.05, 0]^T$ is shown in Fig. 8. The analytical solution to one single inclusion (Eshelby's solution) is $\varepsilon_{22}^E = 2.22e^{-3}$, so that the effective strain in the inclusion increases due to the interaction between inclusions. On the other hand, the effective strain is more concentrated in the center of the inclusion.

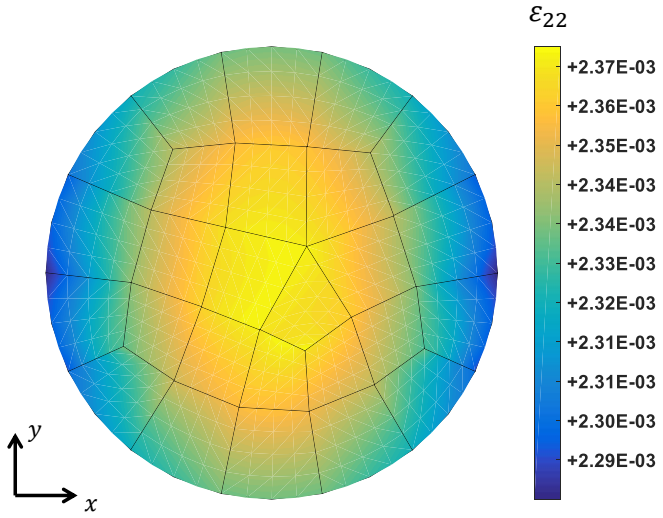

Fig. 8. The distribution of effective strain under $\{\boldsymbol{\varepsilon}^0\} = [-0.02,\ 0.05,\ 0]^T$ (volume fraction 30%, NID 0.04 μm) of a cicular inclusion in 2D.

6.2.1 Volume fraction effect

A study was performed showing the dependence of elastic properties on the volume fraction. The volume fraction ranges from 0% to 55% and 6 replications are prepared for each set of models. It was stated in [17], that the Hashin-Shtrikman lower bound actually coincides to Mori-Tanaka method if all the inclusion are aligned and similarly shaped. As a result, the elastic properties predicted by Mori-Tanaka method are equal to those given by the Hashin-Shtrikman upper and lower bounds. Fig. 9 shows comparison among DNS, SVIM, self-consistent method, Hashin-Shtrikman upper and lower bounds for

effective transverse Young's modulus and Poisson's ratio. Since Hashin-Shtrikman bounds are energy based and Poisson's ratio is not linearly dependent on energy, they are not provided as bounds for Poisson's ratio.

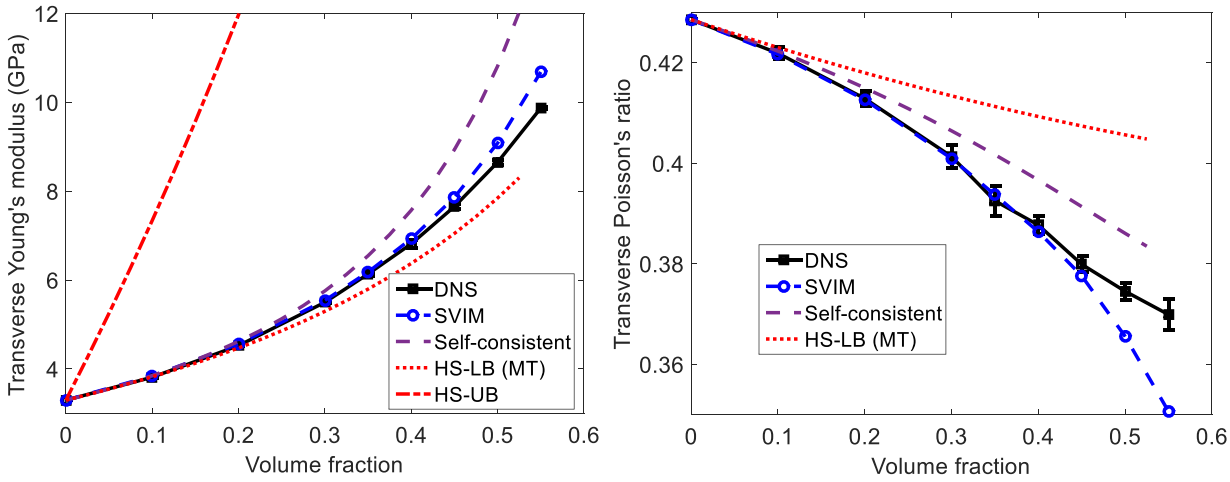

Fig. 9. Effective transverse Young's modulus and Poisson's ratio versus volume fraction given by 2D DNS (direct numerical simulation), SVIM (self-consistent volume-integral micromechanics), self-consistent method, HS-LB and HS-UB (Hashin-Shtrikman lower and upper bounds). MT (Mori-Tanaka) method gives the same result as HS-LB.

As shown in Fig. 9, Mori-Tanaka method always underestimate the transverse Young's modulus and overestimate the Poisson's ratio due to the lack of inclusion interactions. Traditional self-consistent method always overestimate both transverse Young's modulus and Poisson's ratio. The proposed SVIM predictions are close to those of DNS even for high volume fraction above 40%. Usually, Poisson's ratio isn't an easy value to predict in traditional micromechanics methods [29], but SVIM can give a relatively good estimation on Poisson's ratio.

6.2.2 Nearest inclusion distance (NID) effect

Although volume fraction is outstanding factor affecting the properties, it should also be noted that the nearest inclusion distance does affect the overall elastic properties. This is because the nearest inclusion distance changes the stress and strain distributions in the inclusion, as well as in the matrix, with smaller nearest particle distances leading to higher maximum stress and strain values. For traditional micromechanics, such as Mori-Tanaka method and traditional self-consistent method, this phenomenon is generally neglected because the inclusions are not explicitly considered and the morphology of the microstructure is reduced to an effective matrix whose properties are determined by the volume fraction. In this section, we will investigate the influence of the nearest inclusion distance using DNS and SVIM.

A study was performed for models at 30% volume fraction with nearest particle distance varying from 0.01 μm to 0.19 μm. The RVE size is chosen to be 20 μm and 12 replications are generated under each set of control variables (volume fraction and NID). The randomly generated microstructure controlled by the NID 0.01, 0.08 and 0.19 μm are shown in Fig. 10, It can be seen that the inclusions in the model with larger nearest particle distance are more uniformly distributed and the microstructure is closer to a regular structure, so that the spatial variation of the volume fraction is smaller.

The radial distribution functions of the models with NID 0.01, 0.08 and 0.19 μm are plotted in Fig. 11. The NID is equal to the minimum distance corresponding to a non-zeros $g(r)$. Since the microstructure

with larger nearest inclusion distance is closer to the regular structure, higher peaks are observed in the RDF curve which compensate the volume fraction near the center inclusion.

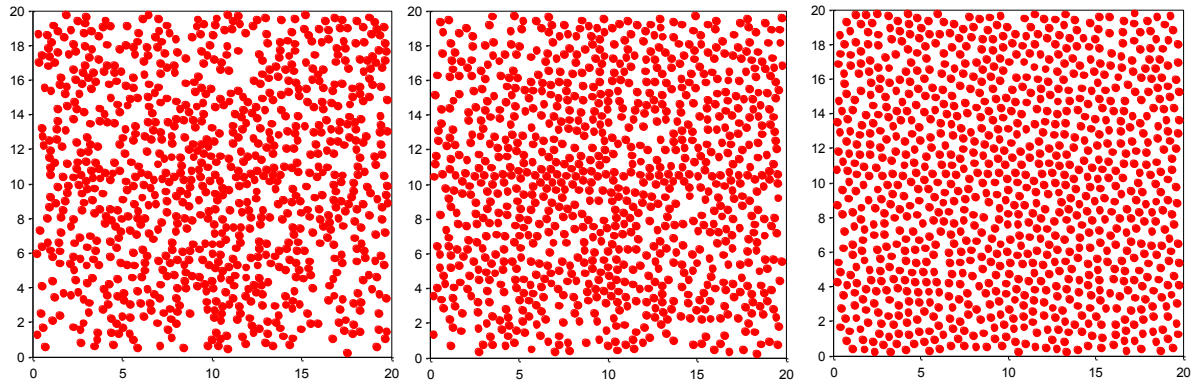

(a) 0.01 μm (b) 0.08 μm (c) 0.19 μm

Fig. 10. The morphologies of the microstructures with nearest distance 0.01, 0.08, 0.19 µm at volume fraction 30% and RVE size 20 µm. The solid dots represent the inclusions in the matrix.

After obtaining the average radial distribution function for each set of models, we can perform the integration numerically using Eq. (43) and use the self-consistent iteration scheme to compute the overall elastic properties. A comparison between the transverse Young's modulus and Poisson's ratio given by the two methods is provided in Fig. 12.

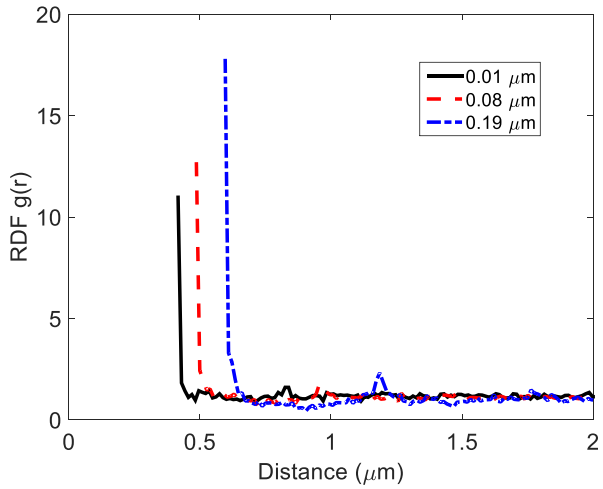

Fig. 11. The RDFs of the microstructures with nearest particle distance 0.01, 0.08, 0.19 µm for volume fraction 30%. The RDFs goes to 1 as the distance increases.

It can be observed in DNS that the effective transverse Young's modulus diminishes with the increasing NID, but the effective transverse Poisson's ratio increases with NID. By collecting RDFs from the RVEs (virtual material), SVIM can also predict the same trend. With NID varying from 0.01 to 0.19 μm, the changes of Young's modulus and Poisson's ratio in DNS are 4.3% and 2.5%, while the changes in SVIM are 2.8% and 1.2%.

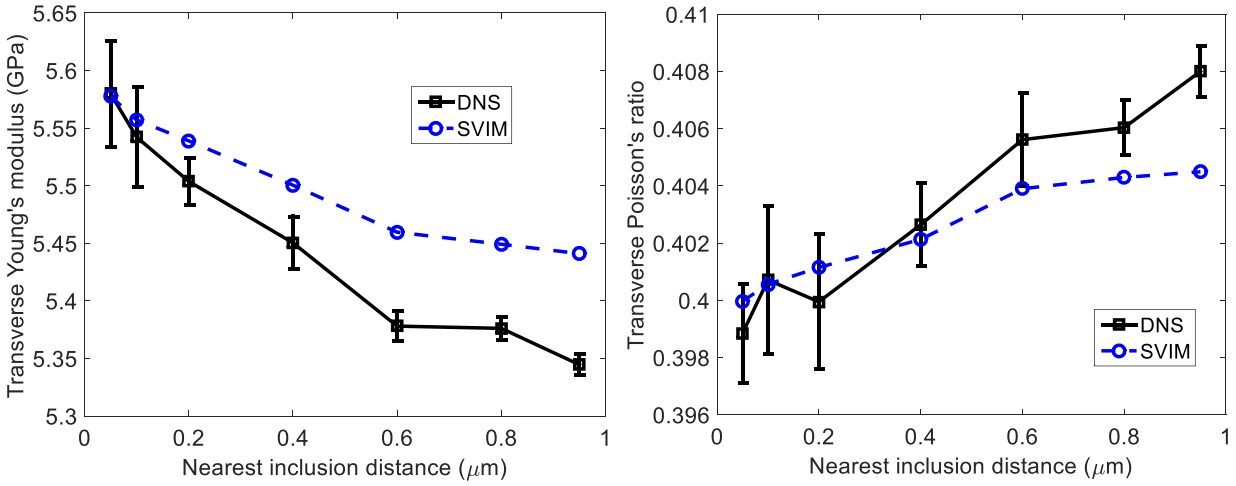

Fig. 12. The nearest inclusion distance effect on the effective transverse Young's modulus and Poisson's ratio given by DNS and SVIM.

6.3 3D problems with spherical inclusions

As mentioned before, 3D DNS is time-consuming and can become intractable as more degrees of freedom are included in the model. In FEA and FFT-based method, the computational time is expected to be proportional to the third order of RVE size. But for SVIM method, the computational times doesn't depend on the RVE size. Most of this computational time is dedicated to integration appearing in the self-consistent equation, which can be parallelized easily. In this section, we will demonstrate SVIM's capability of predicting the effective properties in 3D by comparing results with both DNS and experiments.

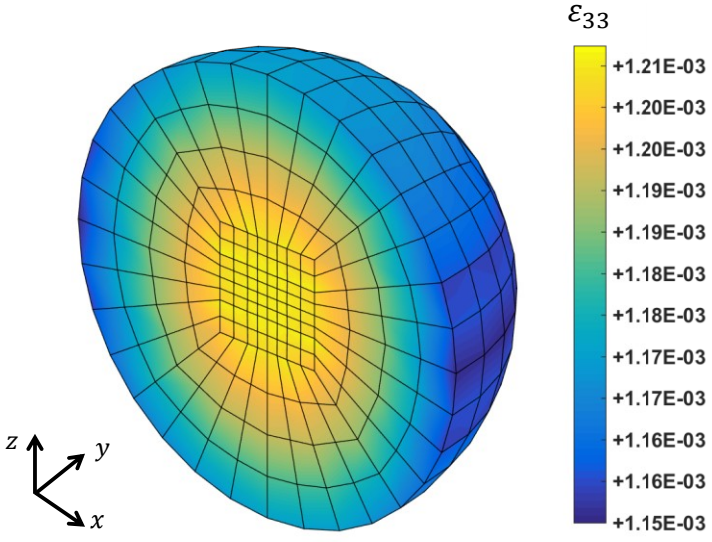

Fig. 13. The distribution of effective strain under $\{\boldsymbol{\varepsilon}^0\} = [-0.02, -0.02, 0.05, 0, 0, 0]^T$ (volume fraction 30%) of a spherical inclusion in 3D.

In the simulations, the elastic properties of the matrix and inclusion materials are $E_m = 1.0$ GPa, $v_m = 0.3$, $E_c = 100$ GPa, $v = 0.3$. The radius of the circular inclusions is equal to 1 μm, and the RVE size is 20 μm. Similarly, RDF of each RVE is calculated and put into the self-consist equation to compute the

effective properties. For a 3D material containing spherical inclusions with volume fraction 30%, the effective distribution of strain ε_{33} in the inclusion under a far field strain $\boldsymbol{\varepsilon}^0$ is shown in Fig. 13. The DNS and SVIM results, together with results from other micromechanics models, are provided in Fig. 14. The results from SVIM matches DNS results very well at all volume fractions.

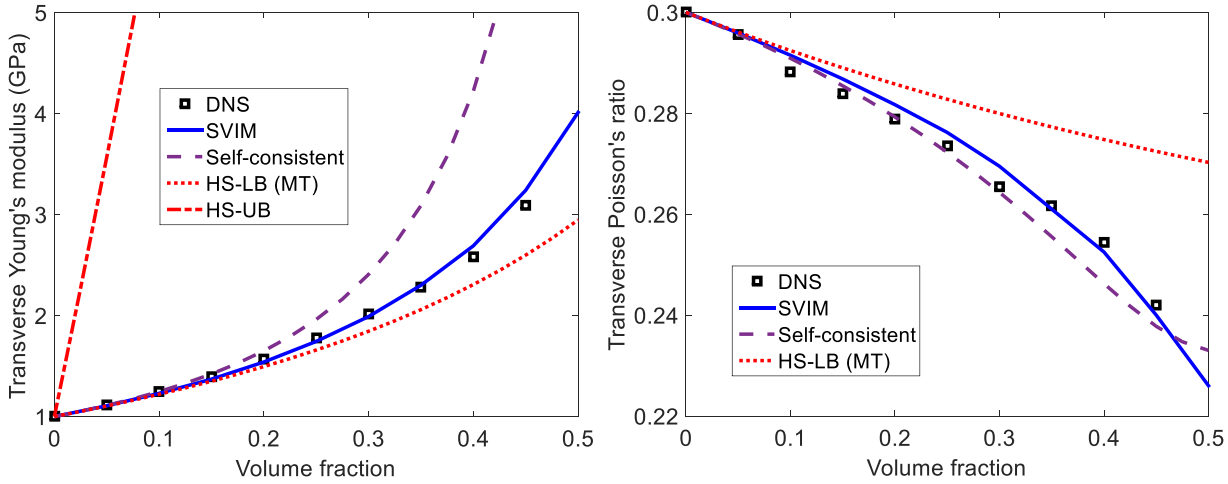

Fig. 14. Effective transverse Young's modulus and Poisson's ratio versus volume fraction given by 3D DNS, SVIM, self-consistent method, HS-LB and HS-UB. MT method gives the same results as HS-LB.

Two experimental studies for two-phase elastic materials with randomly distributed inhomogeneities are used to validate the proposed SVIM method [30, 31]. The elastic properties of the matrix and inclusion material in the two experiments are: 1) $E_m = 3.0$ GPa, $v_m = 0.40$, $E_c = 76$ GPa, $v = 0.23$ from Smith's work [30]; 2) $E_m = 1.69$ GPa, $v_m = 0.444$, $E_c = 70.3$ GPa, $v = 0.21$ from Richard's work [31].

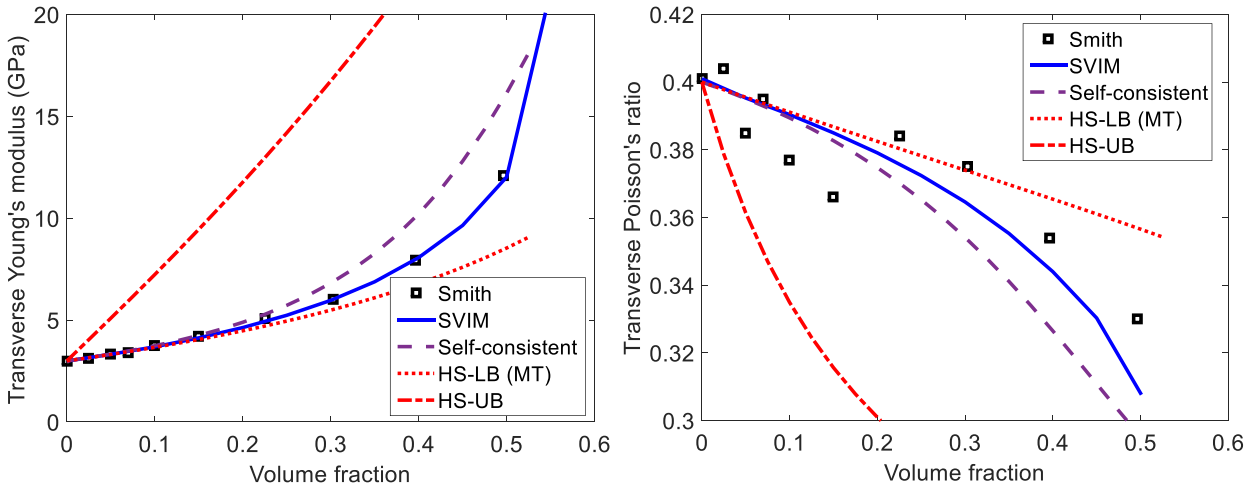

Fig. 15. Effective transverse Young's modulus and Poisson's ratio versus volume fraction from Smith's experiment [30], SVIM, self-consistent method, HS-LB and HS-UB predictions.

Since there is no data of RDF in the experimental work, we will use an RDF given by Percus and Yevick, who obtained an integral equation for $g(r)$ [32]. We will also use Wertheim's work [27], which gives an analytical solution to Percus and Yevick equation, derived under hard sphere assumption, and expressed as a closed-form Laplace transform [27].

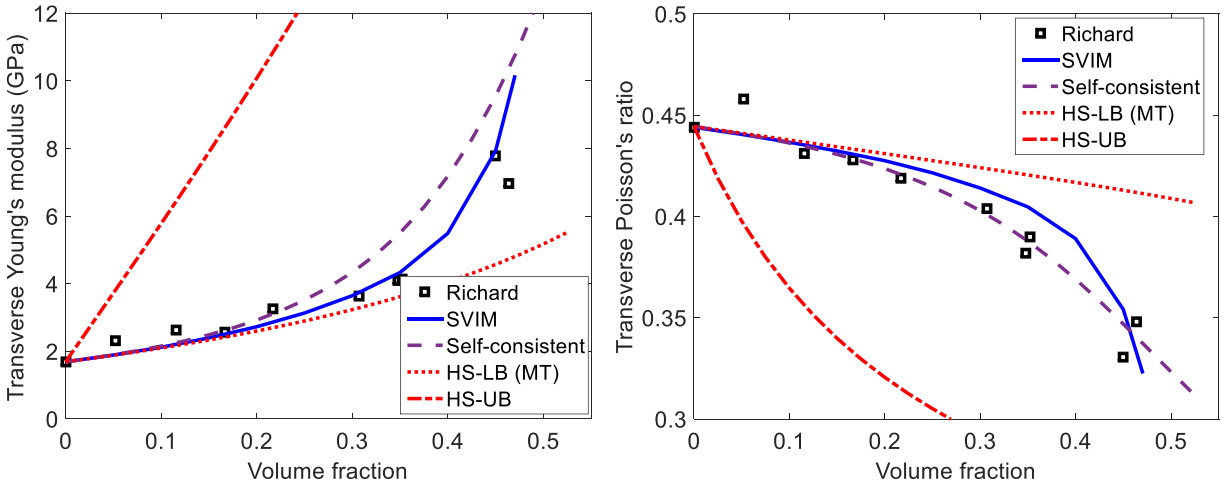

Fig. 16. Effective transverse Young's modulus and Poisson's ratio versus volume fraction from Richard's experiment [31], SVIM, self-consistent method, HS-LB and HS-UB predictions.

For the two sets of material properties, effective transverse Young's modulus and Poisson's ratio predicted by SVIM are provided in Fig. 15 and Fig. 16 respectively. Even at high volume fraction around 50%, SVIM can give a good estimation on the effective material properties.

6.4 Effect of inclusion shapes in 2D

SVIM can consider inclusions with arbitrary shape by discretize the inclusion domain. In this section, we will use SVIM to predict the effective elastic properties of RVEs with different inclusions shapes. The elastic properties of the matrix and inclusion materials are $E_m = 1.0$ GPa, $v_m = 0.3, E_c = 100$ GPa, $v = 0.3$.

As shown in Fig. 17, the first three RVE contains randomly distributed and randomly oriented (a) spherical, (b) potato-shaped, (c) elliptic inclusions, respectively. However, RVE (d) contains randomly distributed, but axis-oriented elliptic inclusions. The aspect ratio of the elliptic inclusion is 4:3. After homogenization, the first three RVEs indicate an isotropic material, while the last one indicates an anisotropic material.

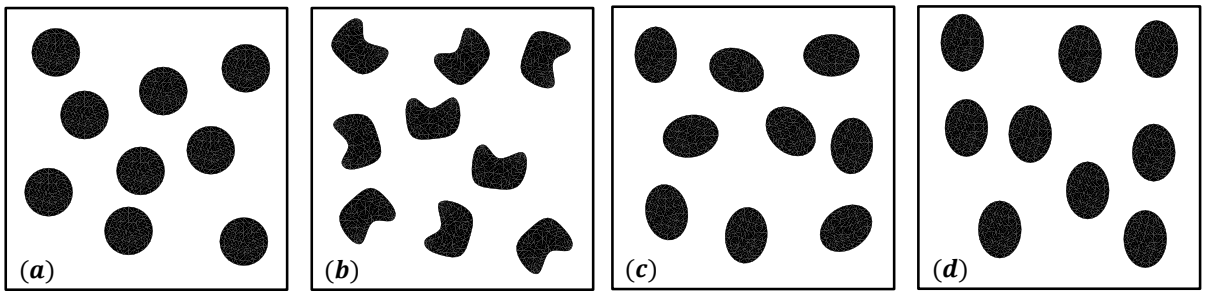

Fig. 17. Illustrations of RVEs with different inclusion shapes.

In SVIM simulations, the RDF comes from the analysis in Section 6.2, and there are around 30 elements in each type of inclusion. For the RVEs with randomly oriented inclusion, the self-consistent equation is modified according to Eq. (34). The effective transverse Young's modulus and Poisson's ratio were

evaluated at volume fractions up to 50%. Since the effective material of RVE (d) is anisotropic, we evaluated it at the two axis-directions of the elliptic inclusion (axis-1 and axis-2).

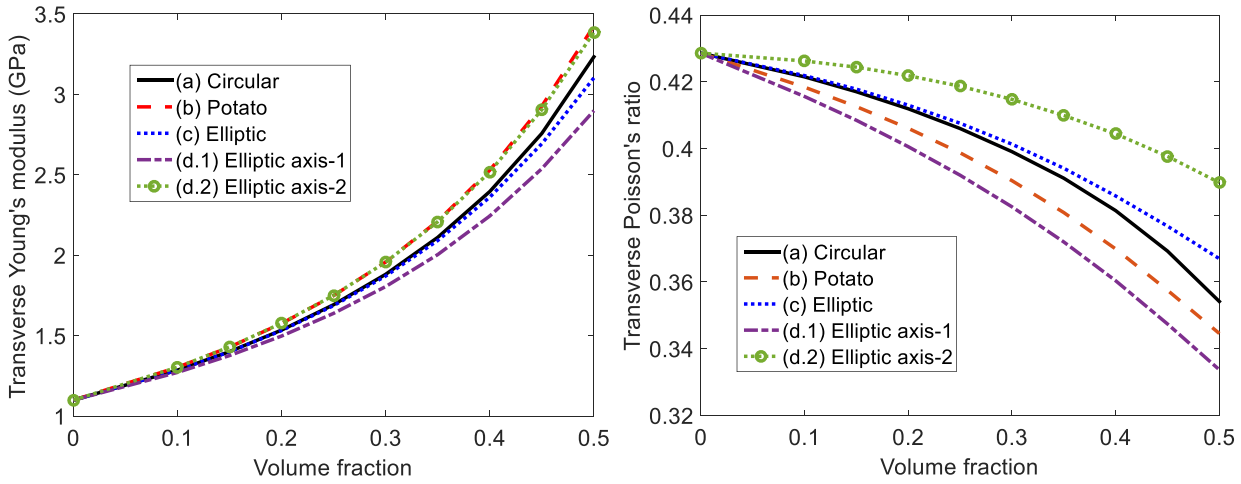

Fig. 18. Effective transverse Young's modulus and Poisson's ratio of material with different inclusions.

For the three isotropic materials (a), (b) and (c), the potato-shaped inclusion gives the largest transverse Young's modulus E_2 and lowest transverse Poisson's ratio v_2, while the elliptic inclusion gives the lowest E_2 and largest v_2. The anisotropic material (d) performs differently. Both of the largest E_2 and v_2 are in axis-2, and the lowest E_2 and v_2 are in axis-1. Based on the predictions given by SVIM, we concluded that the inclusion shape do affect the effective properties.

7. Summary

A procedure using statistical descriptors to predict elastic properties was shown for a virtual two-phase linear elastic material with identical arbitray-shaped non-overlapping inhomogeneities. The study on the nearest particle distance and volume fraction effects for 2D plane strain problems with identical circular no-overlapping inhomogeneities was performed, and it showed the capability of the SVIM method in predicting the overall elastic properties, such as transverse Young's modulus and Poisson's ratio, for various morphologies of the microstructure. SVIM is further extended to 3D problem with identical spherical non-overlapping inhomogeneities. In 3D the SVIM model agreed well with DNS data and captured experimental trends, along with giving more accurate results than traditional micromechanics models. In the end, we used SVIM to investigate the effect of inclusion shape on the effective elastic properties.

While the current work focused only on elastic properties on linear elastic materials, the SVIM method can be extended to viscoelastic material such as polymer composite and plasticity of composite material. Further extensions will allow the SVIM theory to be generalized to consider different geometries of inhomogeneities, multi-phase materials, and anisotropic distributions of the inhomogeneities.

Finally, the computational time of SVIM doesn't depend on the RVE size, and SVIM can also be parallelized conveniently. The advantages in the computational efficiency and high predicting accuracy make the proposed RVE-modeling method a powerful tool for material system design.

Acknowledgement

This project was funded by the Deanship of Scientific Research (DSR), King Abdulaziz University, under grant No. (7-135-1434 HiCi). The authors, therefore, acknowledge technical and financial support of KAU. We are also grateful to Stephen Lin for helpful editing of the manuscript.

Appendix: Green functions in 2D and 3D

For an isotropic linear elastic material in 3D, the Green's function is [33]

$$g_i^j(\mathbf{x}) = \frac{1}{16\pi\mu(1-v)}\left[\frac{x_i x_j}{r^3} + (3-4v)\frac{\delta_{ij}}{r}\right], \text{in 3D,} \tag{46}$$

where $r = \sqrt{x_i x_i}$ with $i = 1, 2, 3$; μ is the shear modulus and v is the Poisson's ratio. Then the derivative of the Green's function is

$$g_{i,k}^j(\mathbf{x}) = \frac{1}{16\pi\mu(1-v)}\left[\frac{x_i}{r^3}\delta_{jk} + \frac{x_j}{r^3}\delta_{ik} - (3-4v)\frac{x_k}{r^3}\delta_{ij} - \frac{3x_i x_j x_k}{r^5}\right], \text{in 3D,} \tag{47}$$

For a 2D linear material under the plane strain condition, the Green's function is

$$g_i^j(\mathbf{x}) = \frac{1}{8\pi\mu(1-v)}\left[\frac{x_i x_j}{r^2} - (3-4v)\delta_{ij}\ln r\right], \text{in 2D plane strain,} \tag{48}$$

where $r = \sqrt{x_i x_i}$, with $i = 1, 2$. Then the derivative of the Green's function is

$$g_{i,k}^j(\mathbf{x}) = \frac{1}{8\pi\mu(1-v)}\left[\frac{x_i}{r^2}\delta_{jk} + \frac{x_j}{r^2}\delta_{ik} - (3-4v)\frac{x_k}{r^2}\delta_{ij} - \frac{2x_i x_j x_k}{r^4}\right], \text{in 2D plane strain.} \tag{49}$$

Reference

[1] G. B. Olson, "Designing a new material world," *Science,* vol. 288, pp. 993-998, 2000.

[2] J. H. Panchal, S. R. Kalidindi, and D. L. McDowell, "Key computational modeling issues in integrated computational materials engineering," *Computer-Aided Design,* vol. 45, pp. 4-25, 2013.

[3] I. Monetto and W. Drugan, "A micromechanics-based nonlocal constitutive equation and minimum RVE size estimates for random elastic composites containing aligned spheroidal heterogeneities," *Journal of the Mechanics and Physics of Solids,* vol. 57, pp. 1578-1595, 2009.

[4] C. Liu, "On the minimum size of representative volume element: an experimental investigation," *Experimental mechanics,* vol. 45, pp. 238-243, 2005.

[5] H. Deng, Y. Liu, D. Gai, D. A. Dikin, K. W. Putz, W. Chen*, et al.*, "Utilizing real and statistically reconstructed microstructures for the viscoelastic modeling of polymer nanocomposites," *Composites Science and Technology,* vol. 72, pp. 1725-1732, 2012.

[6] H. Xu, H. Deng, C. Brinson, D. Dikin, W. K. Liu, W. Chen*, et al.*, "Stochastic reassembly for managing the information complexity in multilevel analysis of heterogeneous materials," in *ASME 2012 International Design Engineering Technical Conferences and Computers and Information in Engineering Conference*, 2012, pp. 199-208.

[7] H. Xu, M. S. Greene, H. Deng, D. Dikin, C. Brinson, W. K. Liu*, et al.*, "Stochastic reassembly strategy for managing information complexity in heterogeneous materials analysis and design," *Journal of Mechanical Design,* vol. 135, p. 101010, 2013.

[8] H. Moulinec and P. Suquet, "A numerical method for computing the overall response of nonlinear composites with complex microstructure," *Computer methods in applied mechanics and engineering,* vol. 157, pp. 69-94, 1998.
[9] J. A. Moore, R. Ma, A. G. Domel, and W. K. Liu, "An efficient multiscale model of damping properties for filled elastomers with complex microstructures," *Composites Part B: Engineering,* vol. 62, pp. 262-270, 2014.
[10] T. Mori and K. Tanaka, "Average stress in matrix and average elastic energy of materials with misfitting inclusions," *Acta metallurgica,* vol. 21, pp. 571-574, 1973.
[11] J. C. Halpin, *Primer on Composite Materials Analysis, (revised)*: CRC Press, 1992.
[12] Z. Hashin and S. Shtrikman, "A variational approach to the theory of the elastic behaviour of multiphase materials," *Journal of the Mechanics and Physics of Solids,* vol. 11, pp. 127-140, 1963.
[13] Z. Hashin, "The elastic moduli of heterogeneous materials," *Journal of Applied Mechanics,* vol. 29, pp. 143-150, 1962.
[14] J. D. Eshelby, "The determination of the elastic field of an ellipsoidal inclusion, and related problems," *Proceedings of the Royal Society of London. Series A. Mathematical and Physical Sciences,* vol. 241, pp. 376-396, 1957.
[15] R. Hill, "A self-consistent mechanics of composite materials," *Journal of the Mechanics and Physics of Solids,* vol. 13, pp. 213-222, 1965.
[16] R. Christensen and K. Lo, "Solutions for effective shear properties in three phase sphere and cylinder models," *Journal of the Mechanics and Physics of Solids,* vol. 27, pp. 315-330, 1979.
[17] J. Ju and T. Chen, "Effective elastic moduli of two-phase composites containing randomly dispersed spherical inhomogeneities," *Acta Mechanica,* vol. 103, pp. 123-144, 1994.
[18] J. Ju and T. M. Chen, "Micromechanics and effective moduli of elastic composites containing randomly dispersed ellipsoidal inhomogeneities," *Acta Mechanica,* vol. 103, pp. 103-121, 1994.
[19] B. Hassani and E. Hinton, "A review of homogenization and topology optimization I—homogenization theory for media with periodic structure," *Computers & Structures,* vol. 69, pp. 707-717, 1998.
[20] R. Hill, "Elastic properties of reinforced solids: some theoretical principles," *Journal of the Mechanics and Physics of Solids,* vol. 11, pp. 357-372, 1963.
[21] Y. Liu, M. Steven Greene, W. Chen, D. A. Dikin, and W. K. Liu, "Computational microstructure characterization and reconstruction for stochastic multiscale material design," *Computer-Aided Design,* vol. 45, pp. 65-76, 2013.
[22] S. Li and G. Wang, *Introduction to micromechanics and nanomechanics* vol. 278: World Scientific, 2008.
[23] K. Tanaka and T. Mori, "Note on volume integrals of the elastic field around an ellipsoidal inclusion," *Journal of Elasticity,* vol. 2, pp. 199-200, 1972.
[24] J. Lee and A. Mal, "A volume integral equation technique for multiple inclusion and crack interaction problems," *Journal of applied mechanics,* vol. 64, pp. 23-31, 1997.
[25] H. B. Li, G. M. Han, and H. A. Mang, "A new method for evaluating singular integrals in stress analysis of solids by the direct boundary element method," *International Journal for Numerical Methods in Engineering,* vol. 21, pp. 2071-2098, 1985.
[26] J.-P. Hansen and I. R. McDonald, *Theory of simple liquids*: Elsevier, 1990.
[27] M. Wertheim, "Exact solution of the Percus-Yevick integral equation for hard spheres," *Physical Review Letters,* vol. 10, pp. 321-323, 1963.
[28] A. Melro, P. Camanho, and S. Pinho, "Generation of random distribution of fibres in long-fibre reinforced composites," *Composites Science and Technology,* vol. 68, pp. 2092-2102, 2008.
[29] J. Segurado and J. Llorca, "A numerical approximation to the elastic properties of sphere-reinforced composites," *Journal of the Mechanics and Physics of Solids,* vol. 50, pp. 2107-2121, 2002.

[30] J. C. Smith, "Experimental values for the elastic constants of a particulate-filled glassy polymer," *J. Res. NBS A,* vol. 80, pp. 45-49, 1976.
[31] T. G. Richard, "The mechanical behavior of a solid microsphere filled composite," *Journal of Composite Materials,* vol. 9, pp. 108-113, 1975.
[32] J. K. Percus and G. J. Yevick, "Analysis of classical statistical mechanics by means of collective coordinates," *Physical Review,* vol. 110, p. 1, 1958.
[33] A. E. H. Love, *A treatise on the mathematical theory of elasticity*: Cambridge University Press, 2013.